

1 **Dynamics of landfalling atmospheric rivers over the North Pacific**
2 **in thirty years of MERRA reanalysis**

3 **ASHLEY E. PAYNE * GUDRUN MAGNUSDOTTIR**

Department of Earth System Science, University of California, Irvine

* *Corresponding author address:* Ashley E. Payne, University of California, Irvine, Department of Earth System Science, 3200 Croul Hall, Irvine, CA 92697.

E-mail: aepayne@uci.edu

ABSTRACT

4
5 A large-scale analysis of landfalling atmospheric rivers (ARs) along the west coast of North
6 America and their association with the upper tropospheric flow is performed for the extended
7 winter (November through March) for the years 1979 to 2011 using MERRA reanalysis
8 data. The climatology, relationship to the El Niño - Southern Oscillation and the Madden -
9 Julian Oscillation, and upper-level characteristics of approximately 750 landfalling ARs are
10 presented based on the 85th percentile of peak daily moisture flux. AR occurrence along the
11 West Coast is dominated by early season events. In composites of upper level fields during
12 AR occurrences, certain characteristics stand out irrespective of the tropical climate indices.
13 This suggests that extratropical dynamical processes play a key role in AR dynamics.

14 The influence of the large scale circulation on AR intensity prior to landfall is examined
15 by objectively selecting an extreme subset of 112 landfalling AR dates representing the
16 95th percentile of strongest cases. Each landfalling AR date that is identified is traced
17 backwards in time using a novel semi-automated tracking algorithm based on spatially and
18 temporally connected organized features in integrated moisture transport. Composites of
19 dynamical fields following the eastward progression of ARs show a close relationship between
20 the location of the jet, Rossby wave propagation and anticyclonic Rossby wave breaking in
21 the upper troposphere of the east Pacific and moisture transport in the lower troposphere.
22 Comparison between the strongest and the weakest ARs within our extreme subset shows
23 differences in both the intensity of moisture transport and the scale and development of
24 anticyclonic Rossby wave breaking in the east Pacific.

1. Introduction

Atmospheric rivers (ARs) are filamentary features with high water vapor content in the lower troposphere that are important for the poleward transport of atmospheric moisture globally (Zhu and Newell 1998). They develop on synoptic timescales, generally in association with low-level moisture convergence within extratropical cyclones, and appear as spatially narrow plumes of moisture that can stretch over thousands of kilometers in the lower troposphere. While ARs form in association with the warm conveyor belt of extratropical cyclones, they are not necessarily uniquely associated with a single cyclone, and an AR can span the lifetimes of multiple cyclones (Newman et al. 2012; Sodemann and Stohl 2013).

AR formation in the northern Pacific basin is of particular interest due to their well-documented effects on land. Along the western coastline of North America, ARs have been connected to heavy precipitation, flooding and snow pack variability when they cross over land (so called landfall) (Ralph et al. 2006; Neiman et al. 2008a; Smith et al. 2010; Dettinger et al. 2011; Guan et al. 2012). Their landfall is important to water resources, particularly within the contiguous United States, where they have been shown to contribute between 30% and 50% of wet season precipitation (Guan et al. 2010; Dettinger et al. 2011). Up to three quarters of persistent droughts along the West Coast have been ended by a landfalling AR storm (Dettinger 2013). Although they operate on rather short timescales, depending on their intensity and synoptic characteristics upon landfall, a relatively small number of these storms can be the difference between dry and wet years (Dettinger et al. 2011; Dettinger 2013).

Despite well documented hydrological impacts and meteorological characteristics of landfalling ARs, the large-scale flow influencing ARs prior to landfall is still an area of active research and has received much attention recently (Ralph et al. 2011; Guan et al. 2010, 2012, 2013; Lavers et al. 2012). In animations and in snapshots of moisture transport over the world's ocean basins as seen in the reanalysis data that we use, the nearly constant presence

52 of ARs in both hemispheres is striking and this was commented on in early studies (e.g.,
53 Newell et al. 1992, Zhu and Newell 1998). Those ARs that intersect the West Coast and
54 make landfall vary in moisture source region, trajectory and intensity (Neiman et al. 2008b).
55 Knowledge of modulating factors is needed to address current challenges in AR forecasting
56 and projections of their distribution, intensity and frequency with future climate change.

57 Work over the Pacific basin has focused on the roles of El Niño - Southern Oscillation
58 (ENSO), the Madden-Julian Oscillation (MJO), and the Pacific-North American pattern
59 (PNA) in modulating ARs (Higgins et al. 2000; Bao et al. 2006; Ryoo et al. 2013; Mo and
60 Higgins 1998b,a; Jones 2000; Ralph et al. 2011; Guan et al. 2012, 2013). Most of these
61 studies have based their conclusions on correlations between the signatures of ARs on land
62 (such as total rainfall and snow water equivalent) and climate mode indices, rather than
63 direct detection of ARs and the dynamical processes driving them. Very few studies have
64 focused on the evolution of the feature itself over the Pacific prior to landfall. Ralph et al.
65 (2011) performed a detailed case study of the development of a single AR over the Pacific
66 basin and attempted to tie its formation and behavior to changes in moisture availability
67 due to the progression of the MJO in the tropics. In the context of the impacts of ENSO
68 on the background flow, Ryoo et al. (2013) found that moisture transport is modulated by
69 both the strength of the subtropical jet and the location of Rossby wave breaking along the
70 west coast of North America. Both of these studies suggest a role for large-scale dynamics
71 in modulating ARs prior to landfall.

72 The scope of the research on large-scale influences on ARs is limited both by the ability
73 of each study to sample ARs and by the complexity of the multi-scale processes contributing
74 towards AR behavior prior to landfall. Because of these limitations, it is difficult to make
75 sweeping conclusions on the dominant mechanisms contributing to variations in AR behavior
76 prior to landfall. Understanding how large-scale dynamical factors influence ARs over the
77 Pacific in the observational record is essential to our understanding of the role ARs will play
78 in the hydrological cycle in a warmer climate.

79 Here we examine the climatological characteristics of landfalling ARs on the West Coast,
80 defined by the 85th percentile of peak daily moisture transport (Lavers et al. 2012), over the
81 extended winter period from 1979 to 2011. To examine their behavior prior to landfall, we
82 develop a back tracking algorithm based on moisture flux to resolve the progression of ARs
83 across the basin in composites. We detail the dynamical influences on the behavior of an
84 extreme subset of ARs that have been tracked over the Pacific basin in a reanalysis product
85 covering more than thirty years of data. We address the following questions: (1) What is the
86 relationship between ARs and upper-level dynamics? and (2) What influences the intensity
87 of ARs prior to landfall?

88 This paper is organized as follows. Data and methodology for identifying landfalling
89 ARs, as well as selecting the cases that make up our back tracked extreme subset, are de-
90 scribed in sections 2 and 3. In section 4, we provide an overview of the characteristics of
91 landfalling ARs over the extended winter for the years 1979 to 2011. Section 4 also shows
92 the relationship between moisture flux over the basin and upper level dynamics using the
93 extreme subset of ARs. In section 5, we show the connection of AR intensity to Rossby
94 wave propagation and breaking. At the end of section 5, we put our results linking ARs to
95 Rossby wave breaking in context by showing the difference between breaking frequency and
96 extent for landfalling AR dates compared to the climatology for the entire extended winter.
97 The conclusions of this study and their implications are found in section 6.

98 **2. Data**

99 We use the Modern-Era Retrospective Analysis for Research and Applications (MERRA)
100 reanalysis dataset, available starting from 1979 from NASA. Use of the MERRA product
101 has significant advantages as it is of high spatial and temporal resolution and was developed
102 specifically for application to the hydrological cycle (Rienecker et al. 2011). Specific humidity,
103 horizontal winds, and potential vorticity were retrieved from pressure levels at reduced spatial

104 resolution ($1.25^\circ \times 1.25^\circ$) at 3-hrly intervals. Total surface precipitation was retrieved at
105 native spatial resolution ($2/3^\circ \times 1/2^\circ$) at 1-hrly intervals. Precipitation data is converted
106 from units of $\text{kg m}^{-2} \text{ s}$ to units of mm and then averaged every three timesteps. The
107 precipitation data at 3-hrly intervals is linearly interpolated to reduced spatial resolution for
108 use with the moisture and dynamical fields.

109 The behavior of the ARs is examined with respect to both the MJO and ENSO using
110 the daily Real-time Multivariate MJO (RMM) index and the monthly Multivariate ENSO
111 Index (MEI), respectively (Wheeler and Hendon 2004; Wolter and Timlin 1998). MJO
112 activity with a RMM amplitude below 1 is considered too weak to have large-scale impacts
113 on circulation and is not considered in the following analysis. El Niño events are indicated
114 by MEI values greater than 0.5 and La Niña events are indicated by MEI values less than
115 -0.5. For each landfalling AR date, the MJO phase (provided the amplitude is greater than
116 1) and the prevailing state of ENSO are recorded.

117 **3. Methods**

118 *a. AR visualization*

119 As has been pointed out by previous researchers (e.g. Bao et al. 2006, Newman et al.
120 2012), ARs do not represent trajectories of moisture as their name might suggest, but are
121 rather constantly evolving pathways for moisture transport, recycling moisture between the
122 atmosphere and the underlying ocean as they move over basins. Observational researchers
123 have long used vertically integrated water vapor content, also known as total precipitable
124 water measured in centimeters of liquid water equivalent, as a proxy for water vapor transport
125 accomplished in ARs (Ralph et al. 2004, 2005; Neiman et al. 2008b; Jiang and Deng 2011;
126 Wick et al. 2013a,b). However, the use of integrated moisture is primarily motivated by a
127 lack of in situ low-level wind data over oceanic regions. The use of a dynamically consistent
128 reanalysis dataset makes direct investigation of moisture transport possible.

129 We follow the methodology in Lavers et al. (2012) to simplify our analysis and define the
130 magnitude of the vertically integrated moisture flux (MF), as follows:

$$MF(\lambda, \phi, t) = g^{-1} \int_{p_s}^{p_t} q(\lambda, \phi, p, t) |\mathbf{v}(\lambda, \phi, p, t)| dp \quad (1)$$

131 where $|\mathbf{v}|$ is the horizontal wind speed on isobaric surfaces measured in units of m s^{-1} , q is
132 specific humidity measured in units of kg kg^{-1} , g is the gravitational acceleration (9.81 m
133 s^{-2}), p_s is 1000 hPa and p_t is 700 hPa. Over the Pacific basin the influence of the jet stream
134 dominates above 700 hPa, whereas water vapor drops off very quickly with height. While
135 previous researchers have integrated to 300 hPa, we found that vertical integration to 700
136 hPa was appropriate.

137 *b. AR dataset construction*

138 Our focus is on wintertime ARs (November through March), as they have been shown
139 to have higher moisture transport and have greater impacts on land (Neiman et al. 2008b).
140 It is important to note that we exclude the month of October in our selection of landfalling
141 dates. Several significant ARs have made landfall during October, impacting the Pacific
142 Northwest in particular, generally related to recurving transitional tropical cyclones (Lynott
143 and Cramer 1966; Ralph et al. 2011). However, because October is a transition season that
144 has many characteristics of late summer, it is very difficult to detect organized structures in
145 MF over the Pacific basin. The ARs making landfall during October have largely different
146 characteristics in both trajectory and in moisture transport from the ARs making landfall
147 in November through March.

148 For each date between November 1st and March 31st for the years 1979 to 2011, we
149 record two values: (1) peak daily MF and (2) total daily precipitation. These two values
150 are calculated as follows. For each date, daily mean MF and precipitation are isolated over
151 a seven gridpoint region, centered on the western coastline of North America between 20°N
152 and 60°N (Fig. 1a-b). Within the outlined region in Fig. 1a, each variable is averaged in

153 the zonal direction. The blue and orange lines in Fig. 1c show the seven point averaged
154 distributions for MF and precipitation, respectively. For each date, the peak MF and the
155 total precipitation, summed over a seventeen gridpoint window in the latitudinal direction
156 and centered on the peak MF , are recorded (Fig. 1c). Figure 1c shows an example of the
157 seventeen-point range over which precipitation is summed and the values recorded for peak
158 MF and total precipitation for 03 Dec 2007. The two values recorded for each date over the
159 entire time period are illustrated in Fig. 2, which shows the distribution of all dates, sorted
160 according to the peak daily MF (black line) and plotted with each date's total precipitation
161 (light grey line).

162 We use two landfalling AR datasets in our study: (1) a climatology of all landfalling
163 AR dates to impact the western coast of North America between 20°N and 60°N between
164 the years 1979 and 2011 and (2) a backtracked subset of the climatology, isolating only
165 the most extreme AR events to make landfall. The details of our methodology follow,
166 where subsection 1 describes how we define our landfalling AR climatology, subsection 2
167 describes how we isolate an extreme subset of landfalling AR dates from our climatology
168 and subsection 3 details our backtracking methods for the extreme subset of landfalling
169 ARs.

170 1) CLIMATOLOGY

171 We define a climatology of landfalling AR dates using the 85^{th} percentile on peak daily MF
172 (generally following the methods in Lavers et al. (2012)), where landfall is defined by physical
173 proximity to the coastline of North America. Landfalling AR dates are all those dates in the
174 time period with peak daily MF values greater than or equal to the 85^{th} percentile (233 kg
175 $\text{m}^{-1} \text{ s}^{-1}$). The vertical dark grey line in Fig. 2 shows the 85^{th} percentile of peak daily MF ,
176 where all dates to the right are labelled as landfalling AR dates. The green dots in Fig. 2 show
177 the locations of 9 notable landfalling AR events, as listed on NOAA's Earth System Research
178 Laboratory AR information page (<http://www.esrl.noaa.gov/psd/atmrivers/events/>).

179 2) SUBSET OF EXTREME CASES - SELECTION

180 As we are unable to distinguish multi-day landfalling events or examine ARs prior to
181 landfall with the climatology of landfalling ARs just described, case selection becomes nec-
182 essary for in-depth analysis. We objectively isolate a subset of landfalling AR days, that can
183 then be extended backwards in time using our tracking algorithm. We emphasize that no
184 part of our case selection procedure is subjective. While our focus is on the intensity of ARs
185 preceding landfall, rather than on any orographic influences, we recognize the importance
186 of characterizing ARs as extreme precipitation events. Therefore, both peak daily MF and
187 total daily precipitation are used to select landfalling dates for our extreme subset.

188 Two thresholds are used to reduce the sample size for the purposes of a more detailed
189 study and to retain the most extreme events to impact the coast. The 95th percentiles for
190 all dates in the time period are calculated for the peak daily MF and associated total daily
191 precipitation (MF threshold: $305 \text{ kg m}^{-1} \text{ s}^{-1}$, precipitation threshold: 8.24 mm). All dates
192 with peak daily MF and total daily precipitation that fall below the thresholds are discarded.
193 The two thresholds on peak daily MF and total daily precipitation are shown as blue and
194 orange lines, respectively, in Fig 2.

195 A criterion is put in place to eliminate the possibility that the subset is dominated by a
196 few large, slow moving events off the coast. For all dates with values greater than the two
197 thresholds, they must be separated by at least three days. This means that if two days with
198 fewer than 3 days separation have sufficiently high values of peak daily MF and total daily
199 precipitation, the date with the greater peak daily MF is retained and the date with the
200 lower peak daily MF is discarded. Applying this logic, of all dates that had values above
201 the set thresholds (127 dates total), 15 were discarded. Of the 15 dates discarded, 11 dates
202 were part of the same multi-day landfalling AR event as a previously selected date. The 4
203 remaining dates (07 Jan 1990, 02 Feb 1991, 10 Dec 1995, 16 Dec 2002) belong to landfalling
204 AR events directly preceding or directly following previously selected dates.

205 Of the 9 notable landfalling AR events mentioned previously (green dots in Fig. 2), only

206 four events satisfy our criteria on both peak daily MF and total daily precipitation: 11 –
207 24 Feb 1986, 29 Dec – 04 Jan 1996/1997, 29 Dec – 02 Jan 2005/2006 and 06 – 07 Nov
208 2006. These four events, produced some of the largest flooding in the Pacific Northwest over
209 the last 50 years and confirm that our case selection process does indeed isolate the most
210 extreme landfalling ARs. When the month of October is considered, the dates originally
211 selected remain largely the same, with 106 of the selected dates remaining the same and 19
212 dates being added due to October events. With improvements to our tracking methodology
213 (description to follow) we may be able to investigate these transitional season landfalling
214 ARs in the future.

215 3) TRACKING

216 We developed a semi-automated algorithm to track the centroid of each selected AR back
217 in time, over the course of its lifetime. Most previous studies only consider the few days right
218 around AR landfall. Here, our aim is to study the development of the events, expanding the
219 timeline of a single event beyond the few days of its landfall.

220 ARs are visualized over the basin, prior to landfall, using MF imagery with a static
221 threshold of $350 \text{ kg m}^{-1} \text{ s}^{-1}$. This threshold is only meant to separate peaks in MF from
222 background moisture prior to landfall, over the basin, and is not used in any way to define
223 the two datasets previously described. Moderately increasing or decreasing this threshold
224 only changed slightly the number of grid-points attributed to an AR and the location of its
225 centroid, but ultimately did not affect the detection of the feature itself as an intense flux
226 of moisture. For each timestep, connected grid points forming a unified area poleward of
227 23.5°N (focus on the extratropics) and greater than an area threshold of $21,000 \text{ km}^2$ were
228 labelled as an instantaneous snapshot of a single AR (Fig. 3, top panel). The area threshold
229 is chosen to retain only the larger scale features. Characteristics, such as the location of the
230 centroid (the center of mass of the feature) and orientation (the angle between the a line
231 of latitude and the major axis of the feature) of the AR, were recorded at each timestep.

232 It should be noted that this algorithm cannot detect the exact moment of formation of the
233 AR. However, because the focus of our study is to investigate the factors contributing to AR
234 intensity rather than its formation, we consider the identification of its first appearance as
235 an organized feature in the extratropics to be a good approximation.

236 We define the lifetime of an AR to be the series of instantaneous snapshots of connected
237 gridpoints that are linked through time. An example of our process is shown in Fig. 3.
238 Through the process described above, we identify the centroids of each possible AR over
239 the Pacific basin at each timestep. The time-intensive part of our method comes with the
240 manual recording of the selected AR's centroid over each timestep. While an automated
241 method to track connected features in both space and time was developed, it was discarded
242 pending further development because centroid locations attributed to each AR were at times
243 inconsistent. Our criteria for linking centroids over time is as follows: (1) The centroid of
244 the tracked feature at landfall must correspond to the selected landfalling date chosen using
245 the methods described in the previous subsection. (2) The general progression of centroids
246 should be eastwards. There is some east-west jumping in centroid location associated with
247 the addition of remnant moisture to the selected feature, but it is quite minor compared to
248 the overall progression of the feature in time. (3) The centroid of the westernmost feature
249 is selected when two features merge (this can be seen between the 00h and 15h timesteps in
250 Fig. 3).

251 For the 112 AR events tracked using our algorithm, we rank the events in order of weakest
252 to strongest according to each AR's lifetime average of the areal maximum MF recorded at
253 each timestep. This ranking system takes into account the entire AR lifetime rather than only
254 its landfalling intensity and allows us to compare and contrast quantitatively the weakest
255 and strongest ARs in the subset. The lifetime average intensities range from 533 kg m^{-1}
256 s^{-1} to $1001 \text{ kg m}^{-1} \text{ s}^{-1}$. It should be emphasized here that ARs are by definition extreme
257 events and that the 'weak' ARs we refer to in our data subset are those selected ARs with
258 the lowest lifetime average of maximum MF .

259 *c. Composites*

260 All composites in our study are calculated based on the longitudinal position of the AR
261 centroid at each timestep, as regionally centered composites. The grey boxes in the following
262 figures mark out 4 regions: (1) 175°–160°W, (2) 160°–145°W, (3) 145°–130°W, and (4) 130°–
263 115°W. For each AR, variables are first averaged for all centroid values within a given region
264 prior to calculating the composite to avoid double-counting slowly moving ARs. Even though
265 many of the trajectories for the tracked ARs extend over the western Pacific, we limit our
266 composites to the eastern Pacific (the four regions listed above) to avoid over-sampling the
267 longest lived ARs.

268 *d. Rossby wave breaking and diagnosis*

269 Rossby wave breaking (RWB) is defined as the rapid and irreversible overturning of
270 potential vorticity (PV) contours (McIntyre and Palmer 1983). Rossby waves propagate
271 along a strong PV gradient and break when the gradient is weakened, such as in a jet
272 exit region. For composites we use PV on the 200 hPa surface to detect breaking and
273 determine the type of breaking: anticyclonic, in which contours overturn in the SW-NE
274 direction, or cyclonic, in which contours overturn in the NW-SE direction. Breaking type is
275 determined on a case by case basis based on breaking direction (See Fig. 1 in Strong and
276 Magnusdottir 2008). The impact of the breaking events is on forcing of the background flow,
277 often determined to be greater when the spatial scale of the breaking is greater.

278 The location and zonal extent of each breaking event is quantified using a RWB detection
279 algorithm first described in Strong and Magnusdottir (2008b) and adapted to 3-hrly MERRA
280 PV data at 200 hPa (coarsened to a resolution of $2.5^\circ \times 2.5^\circ$ using linear interpolation). With
281 this method, the Northern Hemisphere 200 hPa PV field is divided into 400 bins of equal
282 area of approximately 6.4×10^5 km². For each 3-hrly timestep, we identify the longest

283 circumpolar PV contour considering all contours between 0 and 20 PVU¹ (at an interval
 284 of 0.5 PVU). If overturning is detected (contour crosses a meridian more than once), the
 285 centroid of the breaking ‘bay’ and zonal extent (L , calculated as the degree arc length of
 286 a great circle passing through the centroid and spanning the breaking bay), and contour
 287 on which the breaking is detected are recorded (for details, see appendix in Strong and
 288 Magnusdottir (2008b)). For each bin centered on (λ, ϕ) and numbered $n = 1, \dots, N$, the
 289 relative frequency of breaking (γ) and mean zonal extent of breaking (\bar{L}) are calculated as
 290 follows:

$$\gamma(\lambda, \phi)_n \equiv \frac{1}{T} \sum_{t=1}^T \beta[(\lambda, \phi)_n, t] \quad (2)$$

$$\bar{L}(\lambda, \phi)_n \equiv \frac{1}{\sum_{t=1}^T \beta} \sum_{t=1}^T L[(\lambda, \phi)_n, t] \quad (3)$$

291 where,

$$\beta[(\lambda, \phi)_n, t] = \begin{cases} 1 & \text{if centroid is present} \\ 0 & \text{otherwise} \end{cases} \quad (4)$$

292 and where T is the total number of 3-hrly observations. For each type of breaking (anticy-
 293 clonic and cyclonic), γ quantifies the spatial frequency of breaking for a given time period,
 294 where areas of high breaking frequency typically overlap areas of large zonal extents.

295 4. Characteristics of ARs at landfall

296 a. *Climatology for extended winter*

297 First we consider the landfalling characteristics of ARs off the west coast of North Amer-
 298 ica using daily averages for the extended winter (November through March) 1979 - 2011.
 299 Landfall is defined as physical proximity to land, as shown in Fig. 1a. As described in sec-
 300 tion 3b, our climatology of landfalling ARs is composed of all dates for which at least three

¹1 Potential Vorticity Unit (PVU) $\equiv 10^{-6} \text{ m}^2 \text{ s}^{-1} \text{ K kg}^{-1}$

301 gridpoints in the zonal direction, within the boxed region of Fig. 1, have peak daily MF
302 values greater than a set threshold based on the 85th percentile. Of the 4992 dates in the
303 entire time period, 749 are retained as landfalling AR dates. Of the 128 AR dates listed
304 in the climatology in Neiman et al. (2008b), 77 are contained in our climatology and an
305 additional 16 occur in close proximity (less than or equal to ± 2 days) to dates in our clima-
306 tology. Moreover, a number of ARs identified in our study are not included in the Neiman
307 climatology. Differences between the two climatologies are likely attributable to different
308 definitions of AR landfall and the use of MF rather than integrated water vapor, as was used
309 in Neiman et al. (2008b). The 749 dates contain all of the most recent notable landfalling
310 AR events (seen in Fig. 2).

311 The largest number of landfalling dates occur early in the season. An average of 6.1
312 landfalling dates occurred in November (202 dates total), 5.8 in December (192 dates total),
313 5.2 in January (179 dates total), 3.2 in February (110 dates total) and 1.9 in March (67
314 dates total). The decrease in the number of landfalling dates over the course of the season
315 is in general agreement with the findings in Neiman et al. (2008b) (their Fig. 2), which are
316 based on observations of SSM/I integrated water vapor plumes for 1998 to 2005.

317 Figure 4a shows the seasonal breakdown of landfalling latitude. Landfalling latitudes
318 show a shift equatorward towards the end of the season, from an average latitude in Novem-
319 ber of 45.6°N to a March average of 42.2°N. This shift is also seen in landfalling peak daily
320 MF (Fig. 4b). The most intense landfalling AR dates occur in the month of November (302.3
321 $\text{kg m}^{-1} \text{s}^{-1}$) and the weakest occur in the month of March (283.6 $\text{kg m}^{-1} \text{s}^{-1}$). While, associ-
322 ated landfalling total daily precipitation do not show a similar trend (Fig. 4c), precipitation
323 anomalies (based on the daily climatology) show a shift equatorward over the course of the
324 season (not shown).

325 *b. Effects of the MJO and ENSO on ARs*

326 We perform an analysis of the roles of ENSO and the MJO in modulating ARs at landfall
327 using the MEI and RMM indices, respectively. While these large-scale patterns certainly in-
328 fluence the precipitation distribution in the western United States (Ropelewski and Halpert
329 1987; Cayan et al. 1999; Higgins et al. 2000; Jones 2000), our purpose here is to investigate
330 whether they play a direct role in AR behavior at landfall. In our analysis of the MJO, we
331 limit our investigation to amplitudes of the MJO index greater than 1, reducing the number
332 of dates from 749 to 469 landfalling AR dates.

333 The largest number of landfalling dates occur during El Niño (301 dates), the fewest
334 during La Niña (180 dates), and 268 landfalling dates occurring during ENSO neutral con-
335 ditions. Figures 4d-e show the breakdown of landfalling latitude, intensity and precipitation
336 by phase of ENSO. Landfalling latitudes during El Niño events are shifted equatorward, with
337 an average latitude of 43.3°N compared to an average latitude of 45.5°N and 44.9°N for La
338 Niña and neutral phases, respectively. While total precipitation remains similar (Fig. 4f),
339 the poleward shift in landfalling latitude during La Niña events and concentration of positive
340 precipitation anomalies in the Pacific Northwest (not shown) is consistent with wintertime
341 precipitation patterns for the region during La Niña (NOAA Climate Prediction Center).
342 Increased intensity of moisture plumes during ENSO neutral landfalling dates is consistent
343 with previous findings (Higgins et al. 2000; Bao et al. 2006). Landfalling intensities for El
344 Niño and La Niña dates show little difference (Fig. 4e).

345 Figure 5 shows the composite anomalies of 200 hPa zonal wind (dark grey contours)
346 and PV (light grey contours), and the composite anomalies of MF (shaded) for each phase
347 of ENSO. Anomalies are calculated from the daily climatology for each variable and only
348 significant MF anomalies are shown (calculated at the 95% level using Student's t-test).
349 Comparison of Figs. 5a and 5c show a clear equatorward shift in the zonal wind during El
350 Niño dates that is in agreement with Fig. 4d. Significant MF anomalies during El Niño
351 dates cover the entire coastline from Mexico to Alaska. The significant composite anomaly

352 does not extend south of 35°N during La Niña and neutral dates. Warm phase positive pre-
353 cipitation anomalies mirror the meridionally extended range of MF anomalies (not shown),
354 consistent with wintertime precipitation patterns during El Niño (NOAA Climate Prediction
355 Center). The most noticeable difference between the different parts of Fig. 5 is in the zonal
356 wind anomalies. El Niño landfalling dates are associated with an equatorward shifted jet.
357 This suggests that the major role ENSO plays in modulating landfalling ARs is through
358 influence on the position of the jet, which affects the location of the Rossby wave breaking
359 region, as will be discussed in Section 4c.

360 Figures 4g-i show the breakdown of landfalling latitude, intensity and precipitation by
361 phase of the MJO. There are two local maxima in the overall number of landfalling AR dates
362 by phase (not shown). The largest number of landfalling AR dates occur during phase 6 (84
363 dates) and increased activity in phases 7 and 8 (71 dates each), and a smaller secondary peak
364 occurs at phase 3 (62 dates). The peak in AR activity in association with phase 3 (when
365 tropical convection is over the Indian Ocean) and the phase 7-8 increases are consistent with
366 findings in Jones (2000). The peak at phase 6 is consistent with the increase in AR activity
367 described in Guan et al. (2012). While there is no clear trend in landfalling latitude, phases 2
368 and 5 have the most extreme equatorward (40.9°N) and poleward (46.0°N) mean landfalling
369 latitudes, respectively (Figs. 4a,d,g). The two peaks in the number of landfalling AR dates
370 are approximately reflected in precipitation totals, with phase 3 showing the largest average
371 at 7.3 mm and phase 5 showing the smallest average at 6.4 mm (Fig. 4i), consistent with
372 wintertime precipitation patterns for the western United States (NOAA Climate Prediction
373 Center).

374 Figure 6 shows 200 hPa zonal wind (dark grey contour) and PV (light grey contour) com-
375 posite anomalies, and MF (shaded) composite anomalies for each phase of the MJO, showing
376 only statistically significant MF anomalies. We find that positive precipitation anomalies
377 shift approximately poleward from phase 1 to phase 8 (not shown), with the exception of
378 phases 2 and 7. While all phases of the MJO show the presence of a statistically significant

379 moisture anomaly, the anomaly for phase 2 is weak and spread out. It is the most equa-
380 torward reaching, consistent with the very low landfalling latitude and low intensity shown
381 for phase 2 in Figs. 4g-h. The largest positive MF anomaly is in phase 7, which shows the
382 presence of strong, equatorward zonal wind anomalies very similar to Fig. 5c, the El Niño
383 composite. Phase 8, which has the largest landfalling intensity and precipitation total from
384 Fig. 4h-i, also shows eastward extended zonal wind anomalies, consistent with higher latitude
385 positive precipitation anomalies (not shown). MJO phases 3 and 7 have similar landfalling
386 latitudes, intensities and precipitation patterns (not shown).

387 A strong common characteristic between AR composites during ENSO and MJO phases
388 is the presence of a perturbed PV field in the eastern Pacific, in the location of the jet exit
389 region, as indicated by the negative PV anomalies centered over the coastline in Figs. 5
390 and 6. The composites in this section suggest that, while ARs may be modulated by tropi-
391 cal influences on the extratropics, AR variability is ultimately strongly tied to extratropical
392 dynamical mechanisms. This common characteristic motivates our investigation of the dy-
393 namical mechanisms modulating ARs.

394 *c. Dynamical perspective*

395 We consider how landfalling AR dates are different from the mean state. Figure 7 shows
396 composite SLP, 200 hPa PV, 200 hPa wind speed and MF for each winter month for: (a-
397 e) the entire period (1979 – 2011), irrespective of peak daily MF , (f-j) all 749 landfalling
398 AR dates (dates with values above the 85th percentile of peak daily MF), and (k-o) all
399 112 selected AR dates (dates with values above the 95th percentiles of peak daily MF and
400 associated total daily precipitation). Composites in Fig. 7f-j are composed of 202, 191, 179,
401 110 and 67 individual dates, respectively. Composites in Fig. 7k-o are composed of 34, 31,
402 27, 14 and 6 individual dates, respectively.

403 Comparison of the bottom two rows of Fig. 7 with the top row shows a striking departure
404 in the dynamical make-up of AR dates from the climatological mean state over the eastern

405 Pacific in terms of Rossby wave dynamics. The top row shows an unperturbed jet, with an
406 associated largely zonal PV field and unremarkable *MF*. For each month (each column), the
407 two AR rows, show that associated with the strong, lower tropospheric *MF* (which defines the
408 ARs), the PV field and the jet are deformed to a varying extent, manifesting that Rossby
409 wave breaking is taking place. While each frame is an average over many cases, one can
410 still see evidence of overturning PV contours and, thus, Rossby wave breaking (or nonlinear
411 Rossby wave behavior).

412 All AR dates (the middle and bottom rows of Fig. 7) are associated with a westward
413 retreated jet, large perturbations in the PV field and a clearly defined low pressure center to
414 the north and a weak high pressure center to the south of the jet. The jet is climatologically
415 in its most poleward position in November and shifts equatorward over the course of the
416 season. This shift in the jet is reflected in the equatorward shift in landfalling latitude
417 shown in Fig. 4a. Retreat of the jet maximum westward over the course of the season
418 weakens the PV gradient and allows for distortion of the PV contours in the eastern Pacific.
419 The reduction in the PV gradient is downstream and equatorward of the jet exit region. The
420 relationship between the jet and PV field in the monthly composites is consistent with the
421 findings outlined in Abatzoglou and Magnusdottir (2006) (their Fig.5a-b).

422 Comparing the extreme subset of tracked AR dates (Fig. 7k-o) to all AR dates (Fig. 7f-j),
423 we find that, consistent with the climatology, November has the largest number of ARs with
424 34 events and March has the lowest number with only 6 events. Unlike the climatology,
425 however, the shift equatorward in landfalling latitudes is not apparent (not shown). All
426 months of the extreme subset show evidence of a strongly perturbed jet maximum and
427 breakdown of the PV gradient in the eastern Pacific, both in association with the curvature
428 of the moisture plume close to the surface towards the coastline (Fig. 7k-o). For the extreme
429 subset of ARs (bottom row of Fig. 7), all months show a close relationship between the
430 moisture plume at lower levels and the jet maximum at upper levels. This strong, yet
431 deformed, jet is associated with increased distortion of the PV contours and anticyclonic

432 breaking over all months. While there are no discernible changes in the strength of the high
433 pressure center to the south of the moisture plume, the selected ARs have a much deeper
434 low pressure center to the north.

435 *d. Composites of selected cases over the basin*

436 Moving away from static composites of ARs at landfall, we consider the variability of
437 ARs over the Pacific and their development prior to landfall. Figure 8a shows trajectories,
438 smoothed using a moving average filter, for all 112 ARs selected, colored according to their
439 lifetime intensity. Figure 8b shows the relation of initial longitudinal locations in the ex-
440 tratropics relative to the four regions designated in Fig. 8a (the y-axis has no significance),
441 again, colored according to their lifetime intensity. The AR trajectories lie approximately
442 equatorward of the storm track over the Pacific, consistent with their association with the
443 warm sector of extratropical cyclones (based on visual comparison with Fig. 1 in Hoskins
444 and Valdes 1990 and in Chang and Fu 2002). The strongest ARs have initial locations pri-
445 marily in the western Pacific and the weakest ARs have initial locations generally located
446 more eastwards (Fig. 8b).

447 Using the centroid information recorded for each AR, we investigate the nature of the
448 relationship between Rossby waves in the upper troposphere and ARs in the lower tropo-
449 sphere. Figure 9 shows the composite time evolution of the 200 hPa PV field (dark grey
450 contours), 200 hPa wind speed (red contours), SLP (light grey contours) and MF (shading).
451 The red filled circle indicates the average AR centroid location for each composite. The first
452 two frames of the figure (Figs. 9a-b) depict, in the PV field, the eastward propagation of the
453 Rossby wave with the AR centroid following closely. By Fig. 9c, there is evidence of RWB,
454 which becomes clearer in Fig. 9d in terms of the perturbed PV field. Mirroring the behavior
455 of the PV field and the jet in the eastern Pacific, MF curves poleward just off the coast of
456 North America (Fig. 9c-d).

457 It is important to note that Fig. 9 is a composite over many cases, which will lead to a

458 smoothing out of the PV field. On a case by case basis, the ARs at landfall are typically
459 positioned along the western edge of a breaking bay over the eastern Pacific and termi-
460 nate prior to complete overturning of the PV contours. For most of the cases investigated,
461 the resulting breaking is anticyclonic in nature, apparent in Fig. 9d (although diluted due
462 to averaging). The location of breaking associated with the ARs is consistent with both
463 the position of the ARs on the equatorward (anticyclonic) side of the jet and the wintertime
464 RWB climatology for anticyclonic breaking over the Pacific, downstream of the jet maximum
465 (Strong and Magnusdottir 2008b).

466 5. Intensity differences in selected cases

467 To illustrate the dynamical differences that contribute to variations in AR intensity over
468 the basin in greater detail, we divide our subset of extreme AR events into two groups
469 according to average lifetime intensity. Dates with lifetime intensities exceeding the 90th
470 percentile were chosen as our top dates (11 total with values greater than $858.9 \text{ kg m}^{-1} \text{ s}^{-1}$)
471 and dates falling below the 10th percentile were chosen as our bottom dates (11 total with
472 values less than $612.6 \text{ kg m}^{-1} \text{ s}^{-1}$). Composites for these two groups in the following figures
473 are based on the position of the AR centroid, as in Fig. 9, with strong AR composites on
474 the left and weak AR composites on the right.

475 a. Composites

476 Figure 10 shows the composited time evolution of the 200 hPa PV field (dark grey con-
477 tours), 200 hPa wind speed (red contours), SLP (light grey contours) and MF (shading) of
478 the 11 strongest ARs (a-d) and the 11 weakest ARs (e-h).

479 The progression of the strongest ARs is associated with a sustained upper-level jet, even
480 as RWB is taking place, a deep low pressure center to the north and a well defined and
481 persistent high pressure center to the south (Fig. 10a-d). MF plumes have values in excess

482 of $400 \text{ kg m}^{-1} \text{ s}^{-1}$ and are well supported throughout their lifetime by a strong, co-located
483 upper level jet. Progression eastwards is associated with increased nonlinear behavior in the
484 PV field (overturning of contours in Fig. 10b-d). In Fig. 10d, anticyclonic overturning of PV
485 contours is apparent around 120°W and is concurrent with weakening of the AR plume.

486 Relative to the strongest ARs, the weakest ARs are associated with a weaker jet in the
487 eastern Pacific, as RWB takes place, a shallower low pressure center to the north and the
488 absence of a persistent high pressure center to the south (Fig. 10e-h). The associated ex-
489 tratropical cyclone for the strongest ARs is a much tighter system and stronger than the
490 cyclone associated with the weakest ARs. Comparison of MF between the two groups shows
491 the evolution of a much smaller and weaker AR, with values generally below 350 kg m^{-1}
492 s^{-1} . The PV field remains relatively linear over the central Pacific with the appearance of
493 the ARs. Same as for the strongest ARs, the weakest ARs are preceded by breaking in the
494 eastern Pacific around 120°W . Development of nonlinear behavior in the PV field over the
495 eastern Pacific with AR propagation is delayed and it is less coherent and not as well defined
496 compared to features in the left column (Fig. 10g-h).

497 Both the weakest and strongest ARs are associated with the formation of anticyclonic
498 breaking in the eastern Pacific. However, in the weakest ARs, this effect is muted in the
499 composite, and appears later in their lifecycle (Fig. 10h). While ARs developing in associa-
500 tion with linear Rossby wave propagation were observed, none had intense enough moisture
501 transport off the coast of North America to fit into our extreme subset.

502 *b. Rossby wave breaking*

503 To examine the influence that each type of RWB has on AR intensity, we compare the
504 locations and characteristics of RWB for the strongest and weakest ARs. In general, ARs are
505 much more strongly associated with anticyclonic breaking than cyclonic breaking, especially
506 over the eastern Pacific (i.e. Fig. 10). Cyclonic breaking associated with the progression of
507 ARs over the basin and at landfall is dispersed relative to the location of the AR centroids

508 (not shown). The weakest ARs are associated with an increase in the frequency of cyclonic
509 RWB in the eastern Pacific relative to the strongest ARs (not shown). However, the average
510 zonal extent of cyclonic breaking for both groups generally decrease as the ARs progress into
511 the eastern Pacific. We focus on the influence of anticyclonic RWB on AR intensity for the
512 remainder of this section.

513 To illustrate the influence of anticyclonic breaking on ARs, we investigate the breaking
514 locations in relation to the average position of the AR centroid for the strongest and weakest
515 ARs. Each row of Fig. 11 shows all anticyclonic breaking events that occur simultaneously
516 with the centroid in the region outlined in black (both within the region and east of the
517 region). The sizes of the colored markers are scaled according to the zonal extent of each
518 breaking event. The shading of the markers indicates the PV contour on which overturning
519 is detected in units of PVU. At 200 hPa, breaking is generally detected between 0.5 PVU
520 and 8 PVU, consistent with breaking recorded for the 350K level in Strong and Magnusdottir
521 (2008b).

522 The strong association of ARs with anticyclonic RWB is consistent with position of ARs
523 on the equatorward side of the jet and the location of the wintertime anticyclonic surf zone
524 in the eastern Pacific (Abatzoglou and Magnusdottir 2006; Strong and Magnusdottir 2008b).
525 For the strongest ARs, anticyclonic breaking is almost exclusively limited equatorward of
526 the AR centroid and stays relatively concentrated as the AR moves eastward (Fig. 11a-d).
527 For the weakest ARs, breaking is much more dispersed meridionally and is less concentrated
528 (Fig. 11e-h). The overall frequency of anticyclonic breaking is slightly higher for the weakest
529 ARs, however, there are no apparent trends in the frequency of breaking in each region
530 for either the strongest or weakest ARs. The average zonal extents of the breaking events
531 increase for the strongest ARs (from 9.3 to 10.6 arc length units) and decrease for the
532 weakest ARs (from 10.6 to 9.1 arc length units) as the AR propagates eastwards. For the
533 strongest ARs, anticyclonic RWB becomes more spatially concentrated equatorward of the
534 AR centroid, as the AR approaches landfall (Fig. 11c-d).

535 *c. Anticyclonic RWB characteristics of all landfalling ARs*

536 We extend our results to the entire AR climatology and consider the frequency and extent
537 of anticyclonic RWB for all landfalling AR dates compared to the RWB climatology for the
538 extended winter. Figure 12 shows the relative frequency, γ , and average zonal extent, \bar{L} , for
539 anticyclonic RWB for the climatology for the extended winter (a), all landfalling AR dates
540 (b) and for the selected subset of extreme landfalling AR dates (c), respectively. Accounting
541 for differences in the datasets and the use of the 200 hPa pressure surface, the general
542 location of average zonal extent and breaking frequency are consistent with Strong and
543 Magnusdottir (2008b) (their Fig. 2a). Breaking events at this level are detected between 0.5
544 PVU and 8 PVU, again, generally consistent with the findings in Strong and Magnusdottir
545 (2008b). Comparison of Figs. 12b-c to Fig. 12a shows that the maximum in anticyclonic
546 RWB frequency is shifted eastward, over the coast, for AR dates. The strongest AR dates
547 are associated with a substantially higher frequency of anticyclonic breaking in the eastern
548 Pacific, located over the coastline and slightly equatorward of the relative frequency for all
549 ARs over the time period.

550 **6. Discussion and conclusions**

551 This study uses MERRA reanalysis moisture and dynamical fields to investigate large
552 scale features of ARs at landfall and the role of RWB in modifying their behavior and in-
553 tensity over the Pacific basin prior to landfall. Landfalling ARs are identified as plume like
554 features in MF that are above a threshold determined by the data and in physical proximity
555 to the coastline of North America. We investigate the general characteristics of AR landfall
556 over the extended winter (November through March) over more than three decades (1979
557 to 2011) by setting this threshold to the 85th percentile of peak daily MF averaged over the
558 region defined in Fig. 1a. For a more in-depth investigation, from this dataset of landfalling
559 ARs, we objectively select 112 landfalling AR dates by changing the set threshold to the

560 95th percentiles of peak daily MF and total daily precipitation, again, averaged over the
561 region defined in Fig. 1a. The 112 AR dates include 4 significant AR storms that are well
562 documented in the literature. A tracking algorithm based on MF was developed to expand
563 each landfalling event to its full lifetime, from its first appearance in the extratropics as a
564 persistent feature to its termination after making landfall. Use of this tracking algorithm
565 allows for an investigation of the characteristics of each AR, specifically intensity and the
566 path of its centroid over time.

567 Approximately 15% of the dates are landfalling AR days. The largest and most intense
568 landfalling AR days occur in November, with fewer and less intense ARs later in the season.
569 Latitude of landfall shifts equatorward, with the poleward-most ARs occurring in November
570 and the equatorward-most ARs occurring in March. While there are no seasonal trends in
571 total daily precipitation, positive precipitation anomalies shift equatorward over the course
572 of the season (not shown), in line with the seasonality of extreme precipitation events in the
573 western United States (e.g., Fig. 3 in Ralph et al. 2014).

574 Composites of landfalling AR events show a close relationship between ARs, the 200
575 hPa PV field and the closely associated 200 hPa jet. The most noticeable difference in ARs
576 between the different phases of ENSO is in the latitude of landfall. Most landfalling AR
577 dates occur during El Niño, and the fewest occur during La Niña. The MJO is shown to
578 modulate the intensity of landfalling ARs, as well as, precipitation totals.

579 While seasonality in the jet structure may influence the intensity of ARs prior to land-
580 fall, not all of the most intense ARs make landfall early in the season. Investigation of the
581 upper-level characteristics of the extreme subset of dates tracked over the basin shows some
582 common features, such as an extended strong jet and the formation of RWB in the eastern
583 Pacific (Fig. 7f-j). Focusing on the behavior of the tracked ARs over the basin, the strongest
584 ARs first appear in the extratropics in the western Pacific and their trajectories generally
585 correspond to the equatorward side of the jet. Composites of upper-level fields following the
586 progression of the AR eastwards over the basin, show a close relationship between Rossby

587 wave-activity flux and moisture flux. In general, most of the ARs studied formed in as-
588 sociation with Rossby wave propagation in the central Pacific, eventually terminating as
589 anticyclonic RWB took place in the east Pacific.

590 We focus on the dynamical differences influencing AR intensity prior to landfall by com-
591 paring the strongest dates to the weakest dates in our subset, determined based on the 90th
592 and 10th percentiles of the lifetime intensity of all 112 tracked ARs, respectively. The dif-
593 ferences in the strongest and weakest ARs are apparent in the development and extent of
594 anticyclonic RWB in the east Pacific. The strongest ARs are associated with a well devel-
595 oped anticyclonic breaking ‘bay’ in the east Pacific, a strong, but highly perturbed, jet, a
596 tight low pressure center to the north or northwest and a persistent high pressure center
597 to the south or southeast. The weakest ARs are associated with less extensive RWB, that
598 occurs later in the lifetime of the AR, a less perturbed jet, a shallower low pressure center
599 to the north and the absence of a persistent high pressure center to the south.

600 What emerges from this study is the clear dominant influence of extratropical dynamics
601 in terms of Rossby wave propagation and Rossby wave breaking over the east Pacific on the
602 existence of landfalling West Coast ARs. ARs are associated with strong anticyclonic RWB
603 over the east Pacific. This is a dynamically robust region of the world where anticyclonic
604 RWB has been shown to lead to a positive polarity of the North Atlantic Oscillation far
605 downstream (Strong and Magnusdottir 2008a).

606 Our results present a physical link between the large-scale climate patterns and ARs over
607 the North Pacific. Previous studies have alluded to a connection between climate patterns
608 and ARs based on correlations between signatures of ARs on land and climate pattern in-
609 dices. The physical link is the process of RWB that takes place on a similar time scale as
610 the AR lifetime. We have shown a direct link between RWB and ARs. Thus we conclude
611 that the way in which ARs are modulated by extratropical climate patterns is driven by the
612 interaction of these climate patterns with RWB (Strong and Magnusdottir 2008a; Rivière
613 2010).

614 *Acknowledgments.*

615 We thank the two anonymous reviewers who contributed valuable comments and sugges-
616 tions to improve the manuscript. This work is supported by NSF grant AGS-1206120 and
617 NSF GRF under grant DGE-1321846.

REFERENCES

- 620 Abatzoglou, J. T. and G. Magnusdottir, 2006: Planetary wave breaking and nonlinear re-
621 flection: seasonal cycle and interannual variability. *Journal of Climate*, **19**, 6139 – 6152,
622 doi:10.1175/JCLI3968.1.
- 623 Bao, J.-W., S. A. Michelson, P. J. Neiman, F. M. Ralph, and J. M. Wilczak, 2006: Interpre-
624 tation of enhanced integrated water vapor bands associated with extratropical cyclones:
625 Their formation and connection to tropical moisture. *Monthly Weather Review*, **134** (4),
626 1063 – 1080, doi:10.1175/MWR3123.1.
- 627 Cayan, D. R., K. T. Redmond, and L. G. Riddle, 1999: ENSO and hydrologic extremes in the
628 Western United States. *Journal of Climate*, **12**, 2881 – 2893, doi:10.1175/1520-0442(1999)
629 0122.0.CO;2.
- 630 Dettinger, M., 2013: Atmospheric rivers as drought busters on the U.S. West Coast. *Journal*
631 *of Hydrometeorology*, **14**, 1721 – 1732, doi:10.1175/JHM-D-13-02.1.
- 632 Dettinger, M. D., F. M. Ralph, T. Das, P. J. Neiman, and D. R. Cayan, 2011: Atmospheric
633 rivers, floods and the water resources of California. *Water*, **3** (2), 445 – 478, doi:10.3390/
634 w3020445.
- 635 Guan, B., N. P. Molotch, D. E. Waliser, E. J. Fetzer, and P. J. Neiman, 2010: Extreme
636 snowfall events linked to atmospheric rivers and surface air temperature via satellite mea-
637 surements. *Geophysical Research Letters*, **37** (20), 2 – 7, doi:10.1029/2010GL044696.
- 638 Guan, B., N. P. Molotch, D. E. Waliser, E. J. Fetzer, and P. J. Neiman, 2013: The 2010/11
639 snow season in California’s Sierra Nevada: Role of atmospheric rivers and modes of large-
640 scale variability. *Water Resource Research*, **49**, doi:10.1002/wrcr.20537.

641 Guan, B., D. E. Waliser, N. P. Molotch, E. J. Fetzer, and P. J. Neiman, 2012: Does the
642 Madden-Julian Oscillation influence wintertime atmospheric rivers and snowpack in the
643 Sierra Nevada? *Monthly Weather Review*, **140**, 325 – 342, doi:10.1175/MWR-D-11-00087.
644 1.

645 Higgins, R. W., J.-K. E. Schemm, W. Shi, and A. Leetmaa, 2000: Extreme precipitation
646 events in the western United States related to tropical forcing. *Journal of Climate*, **13** (4),
647 793 – 820, doi:10.1175/1520-0442(2000)013<0793:EPEITW>2.0.CO;2.

648 Jiang, T. and Y. Deng, 2011: Downstream modulation of North Pacific atmospheric
649 river activity by East Asian cold surges. *Geophysical Research Letters*, **38**, doi:10.1029/
650 2011GL049462.

651 Jones, C., 2000: Occurrence of extreme precipitation events in California and relationships
652 with the Madden-Julian Oscillation. *Journal of Climate*, **13** (20), 3576 – 3587, doi:10.
653 1175/1520-0442(2000)013<3576:OOEPEI>2.0.CO;2.

654 Lavers, D. A., G. Villarini, R. P. Allan, E. F. Wood, and A. J. Wade, 2012: The detection of
655 atmospheric rivers in atmospheric reanalyses and their links to British winter floods and
656 the large-scale climatic circulation. *Journal of Geophysical Research*, **117**, doi:10.1029/
657 2012JD018027.

658 Lynott, R. E. and O. P. Cramer, 1966: Detailed analysis of the 1962 Columbus Day wind-
659 storm in Oregon and Washington. *Monthly Weather Review*, **94** (2), 105 – 117, doi:
660 10.1175/1520-0493(1966)094<0105:DAOTCD>2.3.CO;2.

661 McIntyre, M. E. and T. N. Palmer, 1983: Breaking planetary waves in the stratosphere.
662 *Nature*, **305** (5935), 593 – 600, doi:10.1038/305593a0.

663 Mo, K. C. and R. Higgins, 1998a: Tropical influences on California precipitation. *Journal of*
664 *Climate*, **11**, 412 – 430, doi:10.1175/1520-0442(1998)011<0412:TIOCP>2.0.CO;2.

- 665 Mo, K. C. and R. W. Higgins, 1998b: Tropical convection and precipitation regimes
666 in the western United States. *Journal of Climate*, **11** (9), 2404 – 2423, doi:10.1175/
667 1520-0442(1998)011<2404:TCAPRI>2.0.CO;2.
- 668 Neiman, P. J., F. M. Ralph, G. a. Wick, Y.-H. Kuo, T.-K. Wee, Z. Ma, G. H. Taylor, and
669 M. D. Dettinger, 2008a: Diagnosis of an intense atmospheric river Impacting the Pacific
670 Northwest: Storm summary and offshore vertical structure observed with COSMIC satel-
671 lite retrievals. *Monthly Weather Review*, **136**, 4398 – 4420, doi:10.1175/2008MWR2550.1.
- 672 Neiman, P. J., F. M. Ralph, G. A. Wick, J. D. Lundquist, and M. D. Dettinger, 2008b: Mete-
673 orological characteristics and overland precipitation impacts of atmospheric rivers affecting
674 the West Coast of North America based on eight years of SSM/I satellite observations.
675 *Journal of Hydrometeorology*, **9**, 22 – 47, doi:10.1175/2007JHM855.1.
- 676 Newman, M., G. N. Kiladis, K. M. Weickmann, F. M. Ralph, and P. D. Sardeshmukh, 2012:
677 Relative contributions of synoptic and low-frequency eddies to time-mean atmospheric
678 moisture transport, including the role of atmospheric rivers. *Journal of Climate*, **25**, 7341
679 – 7361, doi:10.1175/JCLI-D-11-00665.1.
- 680 Ralph, F., P. Neiman, and G. Wick, 2004: Satellite and CALJET aircraft observations of
681 atmospheric rivers over the eastern North Pacific Ocean during the winter of 1997/98.
682 *Monthly Weather Review*, **132** (7), 1721–1745, doi:10.1175/1520-0493(2004)132(1721:
683 SACAOO)2.0.CO;2.
- 684 Ralph, F. M., P. J. Neiman, G. N. Kiladis, K. Weickmann, and D. W. Reynolds, 2011:
685 A multi-scale observational case study of a Pacific atmospheric river exhibiting tropical-
686 extratropical connections and a mesoscale frontal wave. *Monthly Weather Review*, **139**,
687 1169 – 1189, doi:10.1175/2010MWR3596.1.
- 688 Ralph, F. M., P. J. Neiman, and R. Rotunno, 2005: Dropsonde observations in low-level
689 jets over the Northeastern Pacific Ocean from CALJET-1998 and PACJET-2001: Mean

690 vertical-profile and atmospheric-river characteristics. *Monthly Weather Review*, **133** (4),
691 889–910, doi:10.1175/MWR2896.1.

692 Ralph, F. M., P. J. Neiman, G. a. Wick, S. I. Gutman, M. D. Dettinger, D. R. Cayan, and
693 A. B. White, 2006: Flooding on California’s Russian River: Role of atmospheric rivers.
694 *Geophysical Research Letters*, **33**, 2 – 6, doi:10.1029/2006GL026689.

695 Rienecker, M. M., et al., 2011: MERRA - NASA’s Modern-Era Retrospective Analy-
696 sis for Research and Applications. *Journal of Climate*, **24**, 3624 – 3648, doi:10.1175/
697 JCLI-D-11-00015.1.

698 Rivière, G., 2010: Role of Rossby wave breaking in the west Pacific teleconnection. *Geophys-*
699 *ical Research Letters*, **37**, doi:10.1029/2010GL043309.

700 Ropelewski, C. and M. S. Halpert, 1987: Global and regional scale precipitation patterns
701 associated with the El Niño/Southern Oscillation. *Monthly Weather Review*, **115**, 1606 –
702 1626, doi:10.1175/1520-0493(1987)115<1606:GARSPP>2.0.CO;2.

703 Ryoo, J., Y. Kaspi, D. Waugh, G. Kiladis, D. Waliser, E. Fetzer, and J. Kim, 2013: Impact
704 of Rossby wave breaking on U.S. west coast winter precipitation during ENSO events.
705 *Journal of Climate*, **26**, 6360 – 6382, doi:10.1175/JCLI-D-12-00297.1.

706 Smith, B., S. Yuter, P. Neiman, and D. Kingsmill, 2010: Water vapor fluxes and orographic
707 precipitation over northern California associated with a land-falling atmospheric river.
708 *Monthly Weather Review*, **138**, 74 – 100, doi:10.1175/2009MWR2939.1.

709 Sodemann, H. and A. Stohl, 2013: Moisture origin and meridional transport in atmospheric
710 rivers and their association with multiple cyclones. *Monthly Weather Review*, **141**, 2850 –
711 2868, doi:10.1175/MWR-D-12-00256.

712 Strong, C. and G. Magnusdottir, 2008a: How Rossby wave breaking over the Pacific forces

713 the North Atlantic Oscillation. *Geophysical Research Letters*, **35** (10), 1 – 5, doi:10.1029/
714 2008GL033578.

715 Strong, C. and G. Magnusdottir, 2008b: Tropospheric Rossby wave breaking and the
716 NAO/NAM. *Journal of the Atmospheric Sciences*, **65** (9), 2861 – 2876, doi:10.1175/
717 2008JAS2632.1.

718 Wheeler, M. C. and H. H. Hendon, 2004: An all-season real-time multivariate MJO index:
719 development of an index for monitoring and prediction. *Monthly Weather Review*, **132**,
720 1917 – 1932, doi:10.1175/1520-0493(2004)132<1917:AARMMI>2.0.CO;2.

721 Wick, G. A., P. J. Neiman, and F. M. Ralph, 2013a: Description and validation of an auto-
722 mated objective technique for identification and characterization of the integrated water
723 vapor signature of atmospheric rivers. *Geoscience and Remote Sensing, IEEE Transac-*
724 *tions*, **51**, 2166 – 2176, doi:10.1109/TGRS.2012.2211024.

725 Wick, G. A., P. J. Neiman, F. M. Ralph, and T. M. Hamill, 2013b: Evaluation of forecasts of
726 the water vapor signature of atmospheric rivers in operational numerical weather predic-
727 tion models. *Weather and Forecasting*, **28**, 1337 – 1352, doi:10.1175/WAF-D-13-00025.1.

728 Wolter, K. and M. S. Timlin, 1998: Measuring the strength of ENSO events: How does
729 1997/98 rank? *Weather*, 315 – 324, doi:10.1002/j.1477-8696.1998.tb06408.x.

730 Zhu, Y. and R. E. Newell, 1998: A proposed algorithm for moisture fluxes from atmo-
731 spheric rivers. *Monthly Weather Review*, **126** (3), 725 – 735, doi:10.1175/1520-0493(1998)
732 126<0725:APAFMF>2.0.CO;2.

List of Figures

- 733
- 734 1 Example of the case selection methodology applied to 03 Dec 2007. (a) For
735 each day in the time period considered, daily mean MF ($\text{kg m}^{-1} \text{s}^{-1}$, shaded)
736 and daily mean precipitation (mm, contoured starting at 0.5 mm and increas-
737 ing in intervals of 1 mm) are isolated in the region outlined in black, where (b)
738 shows a straightened image of the two variables within the region. The two
739 variables are then averaged over 7 grid points in the zonal direction, shown
740 in (c). For each day, two values are recorded: the peak in daily mean 7-point
741 averaged MF (blue line, c) and the sum of daily mean 7-point averaged precip-
742 itation over a 17-point range in the latitudinal direction, centered on the peak
743 MF . As an example, for 03 Dec 2007, the boundaries of the 17-point range are
744 shown in the horizontal grey lines in (c) and where the two values recorded
745 are $648 \text{ kg m}^{-1} \text{s}^{-1}$ (peak daily MF) and 16.1 mm (total daily precipitation). 35
- 746 2 The distribution of all dates in our time period (NDJFM, 1979 to 2011) sorted
747 according to the peak daily MF ($\text{kg m}^{-1} \text{s}^{-1}$, black line) and plotted with the
748 associated total daily precipitation (mm, light grey line). The dark grey line
749 shows the 85th percentile and dates to the right of this line are labelled as
750 landfalling AR dates (749 total). Our extreme subset of cases are selected
751 from all landfalling AR dates, with values above both the 95th percentile of
752 peak daily MF (blue line) and the 95th percentile of total daily precipitation
753 (orange line), with at least three days of separation. For validation of this
754 methodology, 9 significant landfalling events (11 – 24 Feb 1986, 29 Dec – 04
755 Jan 1996/1997, 02 – 03 Feb 1998, 16 – 18 Feb 2004, 07 – 11 Jan 2005, 25 – 27
756 Mar 2005, 29 Dec – 02 Jan 2005/2006, 06 – 07 Nov 2006, 06 – 08 Jan 2009)
757 are indicated by green points (multiday events use the date with the highest
758 peak daily MF). 36

- 759 3 (top panel) An example of the tracking algorithm applied to 18:00 UTC 01
760 Dec 2007. (top panel) Separated features are colored in varying shades of pink
761 and the centroid of the AR of interest is marked by a filled black dot. (00h
762 – 45h) Starting from 18:00 UTC 01 Dec 2007, the AR of interest is tracked
763 through time as indicated by the dashed black lines. 37
- 764 4 Probability density functions for landfalling ARs over the extended winter
765 for the years 1979 to 2011 sorted according to: (a-c) month - 749 dates, (d-
766 f) ENSO phase - 749 dates and (g-i) MJO phases with amplitudes greater
767 than one - 469 dates. Each column shows the distribution of: (a,d,g) land-
768 falling latitude, (b,e,h) landfalling peak daily MF and (c,f,i) landfalling total
769 daily precipitation. The y-axis shows the probability density function for each
770 panel, where the center column is an order of magnitude less than the right
771 and left columns. Averages for each category are shown in the legend of each
772 panel. 38
- 773 5 Composite 200 hPa zonal wind anomalies (dark grey contours, intervals of 3
774 m s^{-1}), 200 hPa PV anomalies (light grey contours, intervals of 0.5 PVU), and
775 MF anomalies (shaded, intervals of $10 \text{ kg m}^{-1} \text{ s}^{-1}$), with negative contours
776 dashed, for (a) La Niña - 180 dates, (b) neutral - 268 dates, and (c) El Niño
777 - 301 dates, for all 749 ARs over the extended winter over the years 1979 to
778 2011 (15°N to 65°N , 160°W to 115°W). Anomalies are calculated from the
779 daily climatology of each variable. Statistical significance is calculated using
780 Student's t-test at the 95% level. 39
- 781 6 Same as Fig. 5, but for the MJO, for (a) phase 1 - 38 dates, (b) phase 2 - 49
782 dates, (c) phase 3 - 62 dates, (d) phase 4 - 43 dates, (e) phase 5 - 51 dates,
783 (f) phase 6 - 84 dates, (g) phase 7 - 71 dates and (h) phase 8 - 71 dates, for
784 all 469 ARs over the extended winter over the years 1979 to 2011 with RMM
785 amplitudes greater than 1 (15°N to 65°N , 160°W to 115°W). 40

- 786 7 Composite SLP (light grey contour, intervals of 5 hPa), PV at 200 hPa (dark
787 grey contour, intervals of 1 PVU), wind speed at 200 hPa (red contour, in-
788 tervals of 5 m s⁻¹) and *MF* (shaded) for (a,f,k) November, (b,g,l) December,
789 (c,h,m) January, (d,i,n) February, and (e,j,o) March for (top row) the climato-
790 logical mean of the extended winter over the years 1979 to 2011, (middle row)
791 all 749 ARs over the extended winter over the years 1979 to 2011 and (bottom
792 row) the 112 selected landfalling dates (15°N to 65°N, 160°W to 115°W). 41
- 793 8 (a) Trajectories of all 112 landfalling AR cases, shaded according to lifetime
794 intensity (as described in section 3). The grey boxes in (a) and (b) refer to
795 the same areas and represent the regions over which composites are calculated
796 based on AR centroid location: (1) 175°–160°W, (2) 160°–145°W, (3) 145°–
797 130°W and (4) 130°–115°W. (b) Each point represents the longitude at which
798 the AR is first detected. 42
- 799 9 Composite SLP (light grey contour, intervals of 5 hPa), PV at 200 hPa (dark
800 grey contour, intervals of 1 PVU), wind speed at 200 hPa (red contour, inter-
801 vals of 10 m s⁻¹) and *MF* (shaded) for the 112 AR events in our extreme subset
802 for (a) 175°–160°W, (b) 160°–145°W, (c) 145°–130°W and (d) 130°–115°W.
803 The average location of the AR centroid is marked by a filled red dot. 43
- 804 10 Same as Fig. 9, but for the (a-d) 11 strongest ARs and (e-h) 11 weakest ARs
805 in our extreme subset for (a,e) 175°–160°W, (b,f) 160°–145°W, (c,g) 145°–
806 130°W and (d,h) 130°–115°W. The average location of the AR centroid is
807 marked by a filled red dot. 44

- 808 11 Relationship between the location of the AR (filled black dot) and anticyclonic
809 RWB for the (a-d) 11 strongest and (e-h) 11 weakest ARs. Using the same
810 regions as in Fig. 9, for each panel, the region the AR is in is outlined in black
811 and all breaking occurring within and leading that region is plotted, where
812 shading indicates the position of breaking (PVU) and size indicates its zonal
813 extent. 45
- 814 12 Anticyclonic RWB relative frequency, γ , (contoured, intervals of 0.05 with the
815 0.2 contour bolded) and average zonal extent, \bar{L} , (shaded, units of arc length)
816 for (a) the climatological mean of the extended winter over the years 1979 to
817 2011, (b) all 749 landfalling AR dates over the extended winter over the years
818 1979 to 2011 and (c) the selected subset of 112 extreme landfalling AR dates. 46

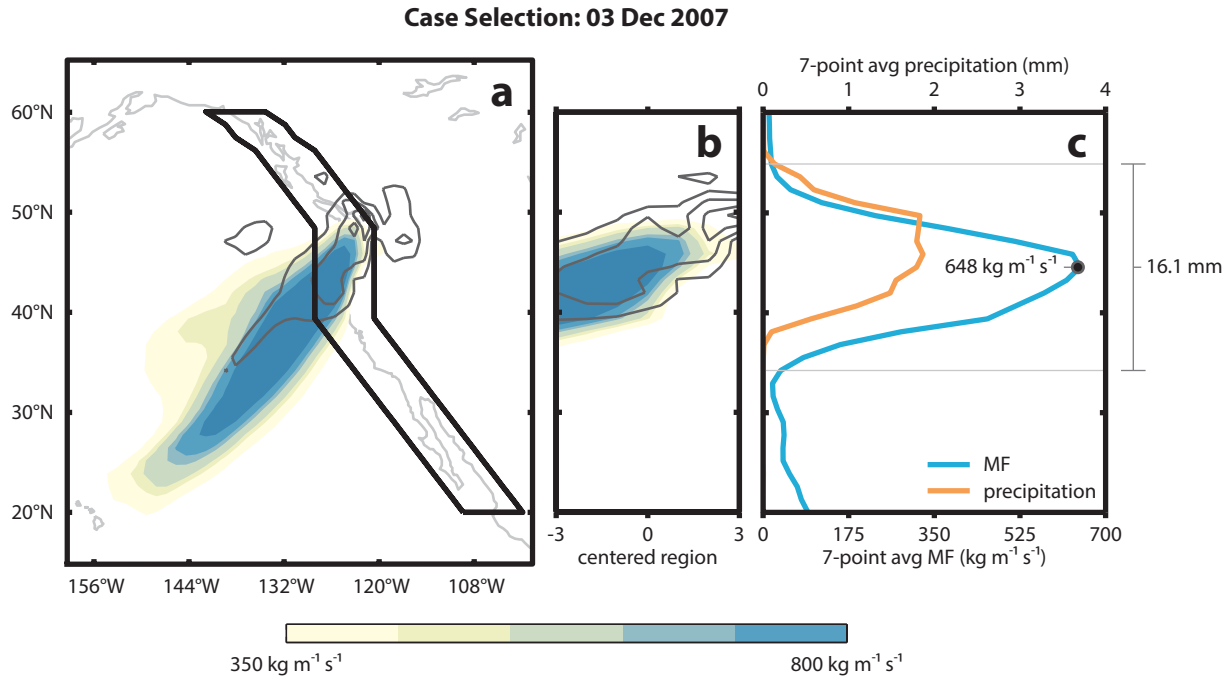


FIG. 1. Example of the case selection methodology applied to 03 Dec 2007. (a) For each day in the time period considered, daily mean MF ($\text{kg m}^{-1} \text{s}^{-1}$, shaded) and daily mean precipitation (mm , contoured starting at 0.5 mm and increasing in intervals of 1 mm) are isolated in the region outlined in black, where (b) shows a straightened image of the two variables within the region. The two variables are then averaged over 7 grid points in the zonal direction, shown in (c). For each day, two values are recorded: the peak in daily mean 7-point averaged MF (blue line, c) and the sum of daily mean 7-point averaged precipitation over a 17-point range in the latitudinal direction, centered on the peak MF . As an example, for 03 Dec 2007, the boundaries of the 17-point range are shown in the horizontal grey lines in (c) and where the two values recorded are $648 \text{ kg m}^{-1} \text{s}^{-1}$ (peak daily MF) and 16.1 mm (total daily precipitation).

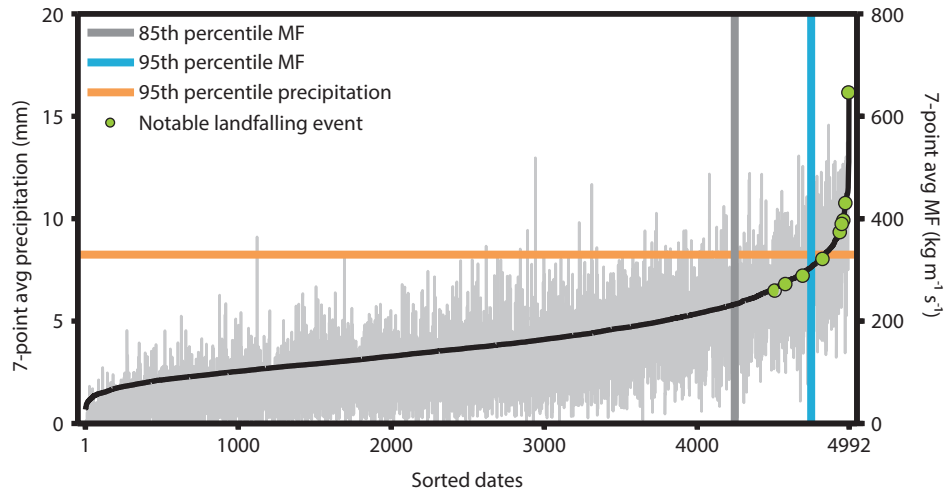


FIG. 2. The distribution of all dates in our time period (NDJFM, 1979 to 2011) sorted according to the peak daily MF ($\text{kg m}^{-1} \text{s}^{-1}$, black line) and plotted with the associated total daily precipitation (mm, light grey line). The dark grey line shows the 85th percentile and dates to the right of this line are labelled as landfalling AR dates (749 total). Our extreme subset of cases are selected from all landfalling AR dates, with values above both the 95th percentile of peak daily MF (blue line) and the 95th percentile of total daily precipitation (orange line), with at least three days of separation. For validation of this methodology, 9 significant landfalling events (11 – 24 Feb 1986, 29 Dec – 04 Jan 1996/1997, 02 – 03 Feb 1998, 16 – 18 Feb 2004, 07 – 11 Jan 2005, 25 – 27 Mar 2005, 29 Dec – 02 Jan 2005/2006, 06 – 07 Nov 2006, 06 – 08 Jan 2009) are indicated by green points (multiday events use the date with the highest peak daily MF).

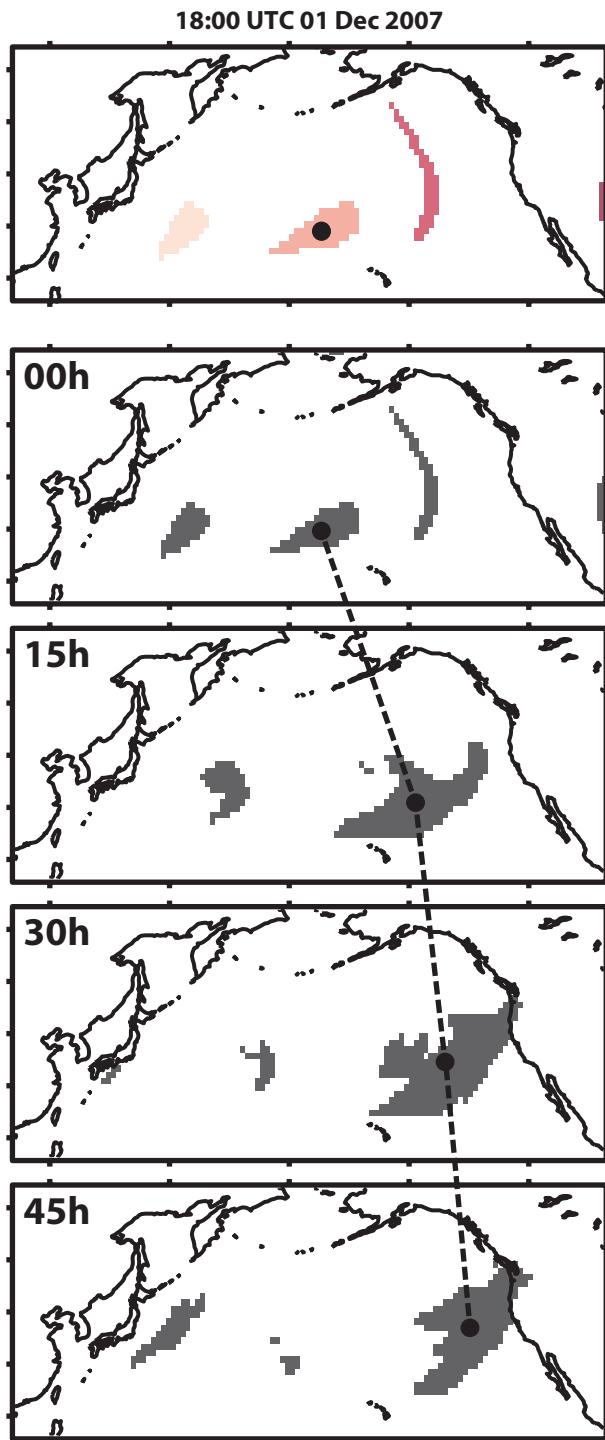


FIG. 3. (top panel) An example of the tracking algorithm applied to 18:00 UTC 01 Dec 2007. (top panel) Separated features are colored in varying shades of pink and the centroid of the AR of interest is marked by a filled black dot. (00h – 45h) Starting from 18:00 UTC 01 Dec 2007, the AR of interest is tracked through time as indicated by the dashed black lines.

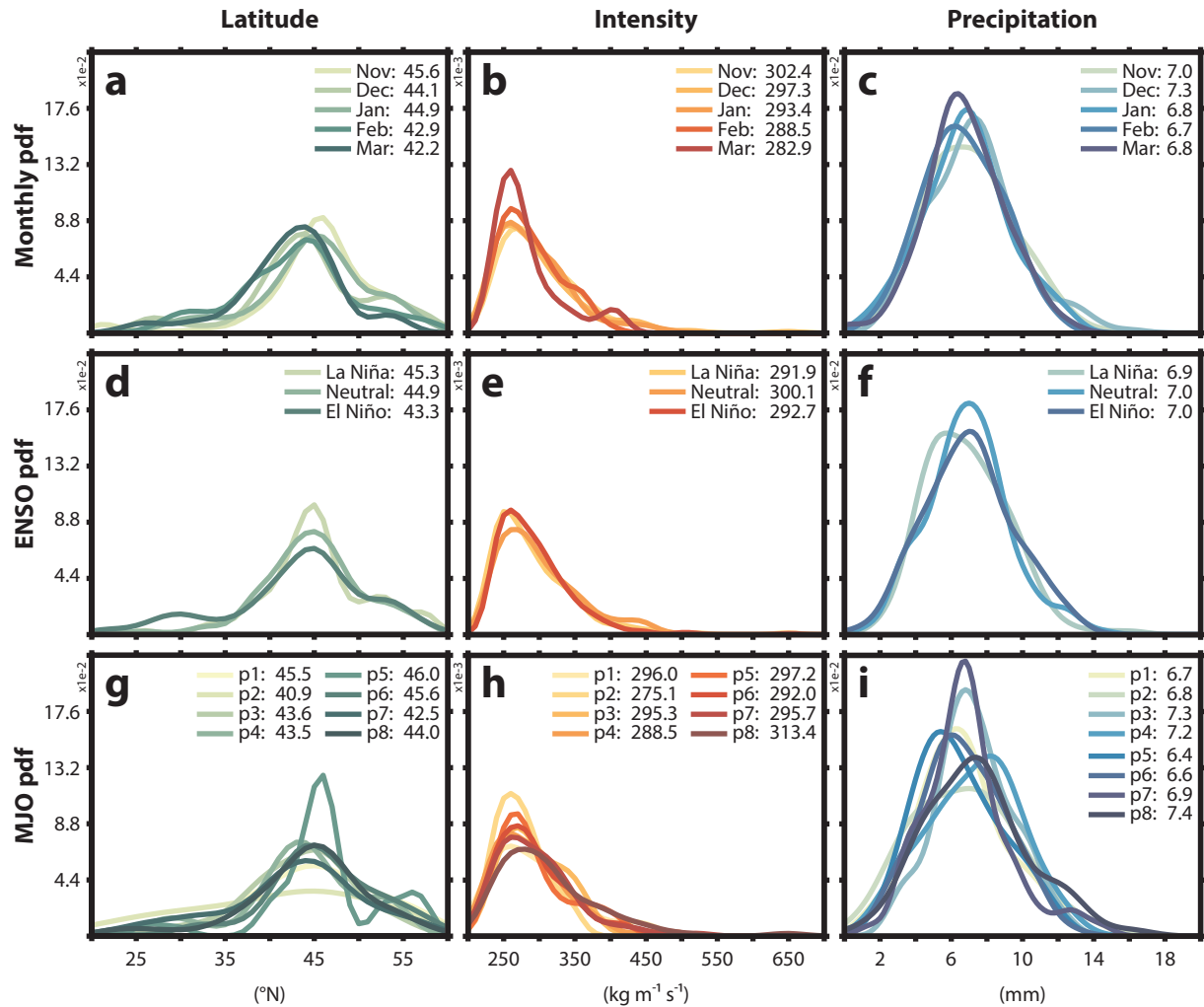


FIG. 4. Probability density functions for landfalling ARs over the extended winter for the years 1979 to 2011 sorted according to: (a-c) month - 749 dates, (d-f) ENSO phase - 749 dates and (g-i) MJO phases with amplitudes greater than one - 469 dates. Each column shows the distribution of: (a,d,g) landfalling latitude, (b,e,h) landfalling peak daily MF and (c,f,i) landfalling total daily precipitation. The y-axis shows the probability density function for each panel, where the center column is an order of magnitude less than the right and left columns. Averages for each category are shown in the legend of each panel.

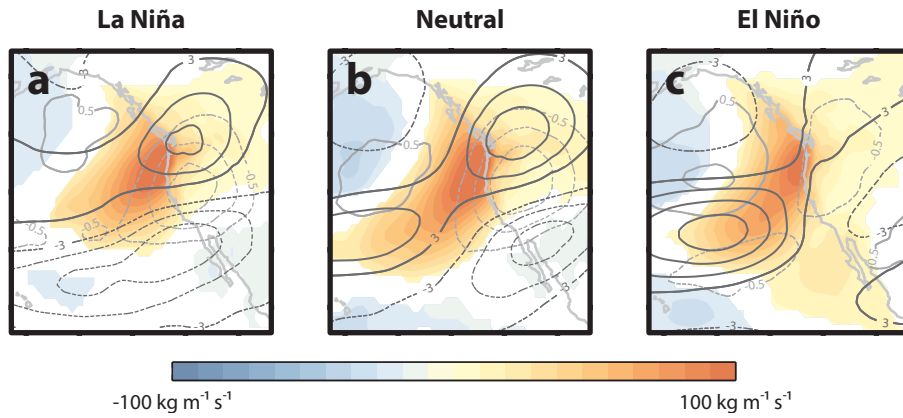


FIG. 5. Composite 200 hPa zonal wind anomalies (dark grey contours, intervals of 3 m s⁻¹), 200 hPa PV anomalies (light grey contours, intervals of 0.5 PVU), and MF anomalies (shaded, intervals of 10 kg m⁻¹ s⁻¹), with negative contours dashed, for (a) La Niña - 180 dates, (b) neutral - 268 dates, and (c) El Niño - 301 dates, for all 749 ARs over the extended winter over the years 1979 to 2011 (15°N to 65°N, 160°W to 115°W). Anomalies are calculated from the daily climatology of each variable. Statistical significance is calculated using Student's t-test at the 95% level.

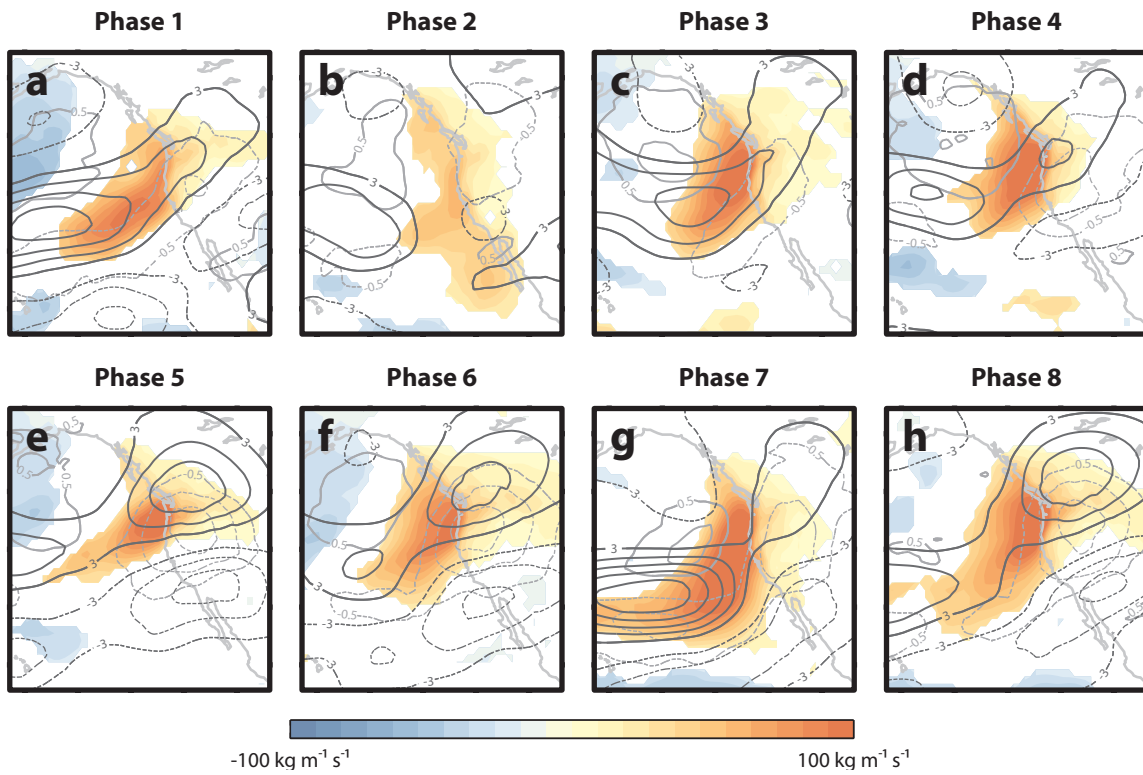


FIG. 6. Same as Fig. 5, but for the MJO, for (a) phase 1 - 38 dates, (b) phase 2 - 49 dates, (c) phase 3 - 62 dates, (d) phase 4 - 43 dates, (e) phase 5 - 51 dates, (f) phase 6 - 84 dates, (g) phase 7 - 71 dates and (h) phase 8 - 71 dates, for all 469 ARs over the extended winter over the years 1979 to 2011 with RMM amplitudes greater than 1 (15°N to 65°N , 160°W to 115°W).

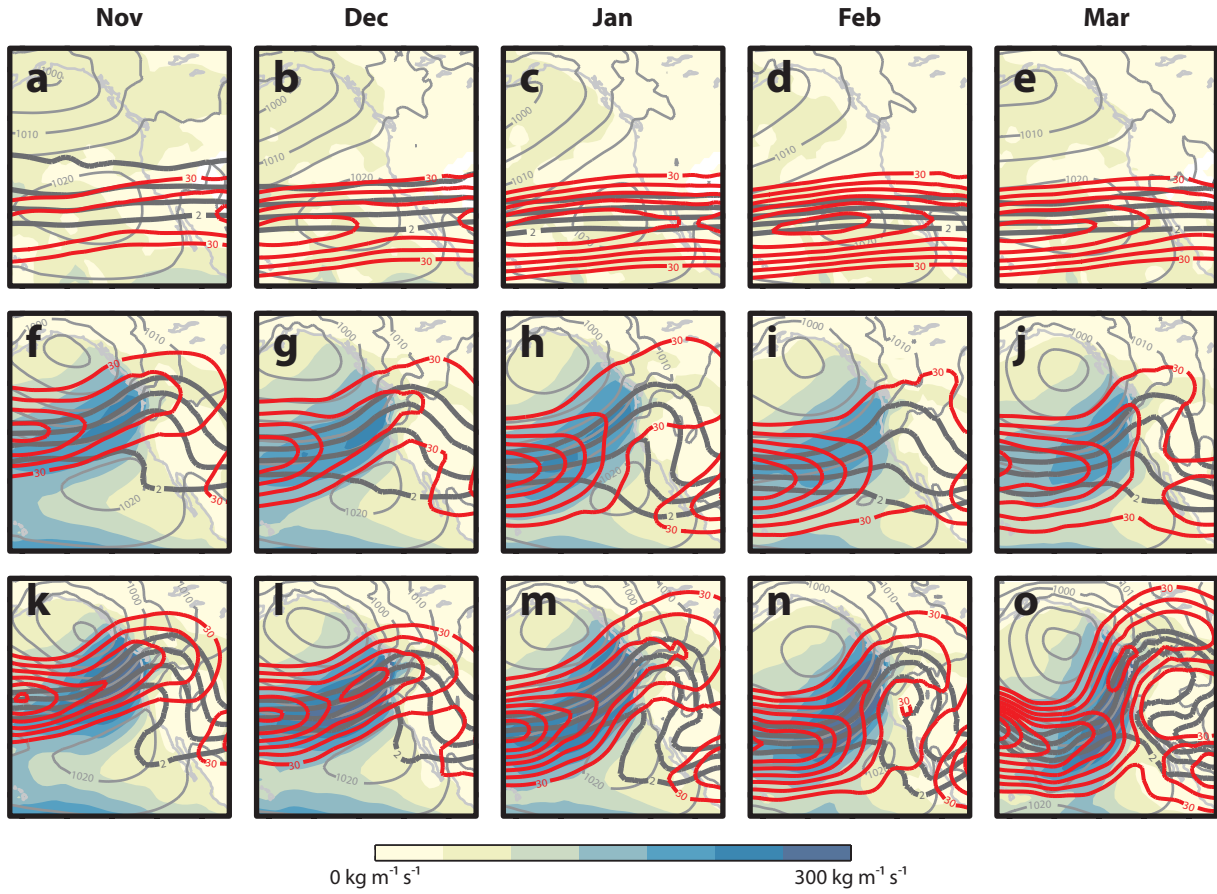


FIG. 7. Composite SLP (light grey contour, intervals of 5 hPa), PV at 200 hPa (dark grey contour, intervals of 1 PVU), wind speed at 200 hPa (red contour, intervals of 5 m s⁻¹) and *MF* (shaded) for (a,f,k) November, (b,g,l) December, (c,h,m) January, (d,i,n) February, and (e,j,o) March for (top row) the climatological mean of the extended winter over the years 1979 to 2011, (middle row) all 749 ARs over the extended winter over the years 1979 to 2011 and (bottom row) the 112 selected landfalling dates (15°N to 65°N, 160°W to 115°W).

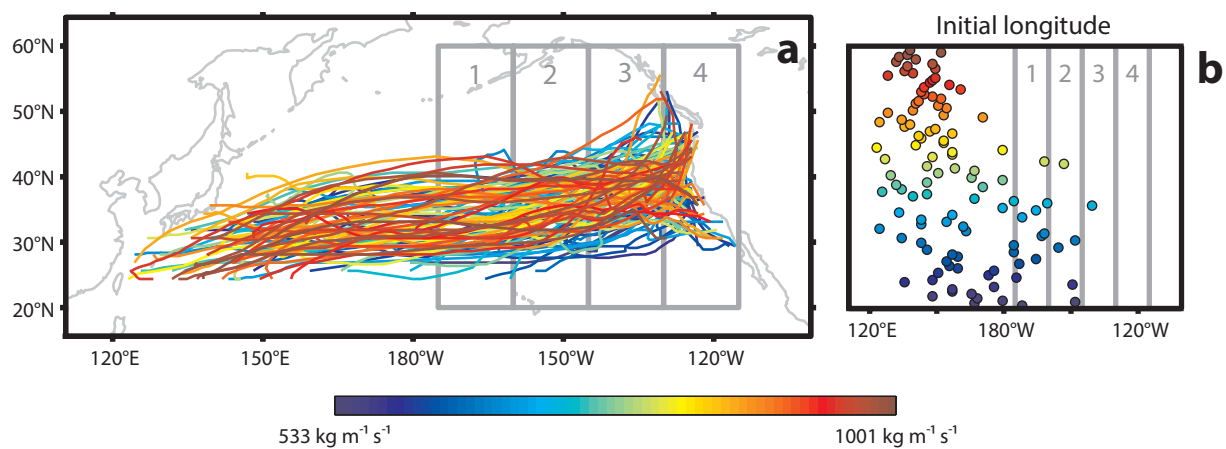


FIG. 8. (a) Trajectories of all 112 landfalling AR cases, shaded according to lifetime intensity (as described in section 3). The grey boxes in (a) and (b) refer to the same areas and represent the regions over which composites are calculated based on AR centroid location: (1) 175°–160°W, (2) 160°–145°W, (3) 145°–130°W and (4) 130°–115°W. (b) Each point represents the longitude at which the AR is first detected.

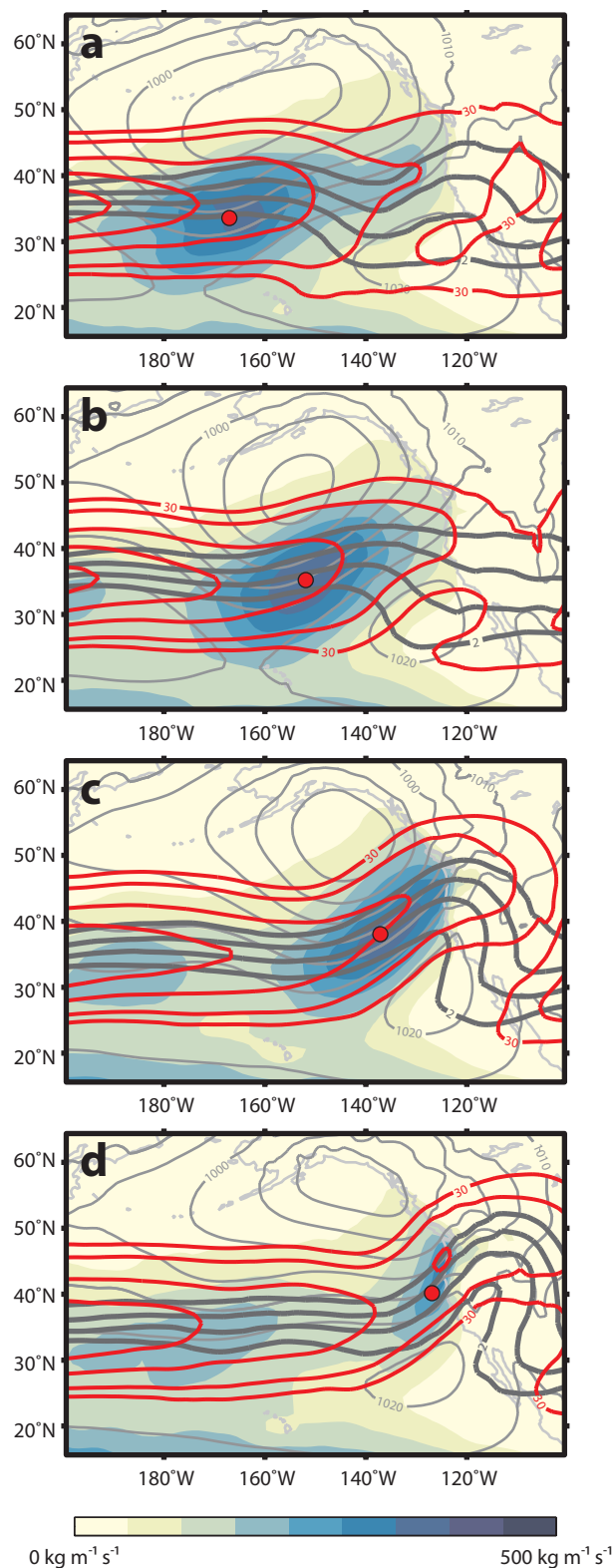


FIG. 9. Composite SLP (light grey contour, intervals of 5 hPa), PV at 200 hPa (dark grey contour, intervals of 1 PVU), wind speed at 200 hPa (red contour, intervals of 10 m s⁻¹) and *MF* (shaded) for the 112 AR events in our extreme subset for (a) 175°–160°W, (b) 160°–145°W, (c) 145°–130°W and (d) 130°–115°W. The average location of the AR centroid is marked by a filled red dot.

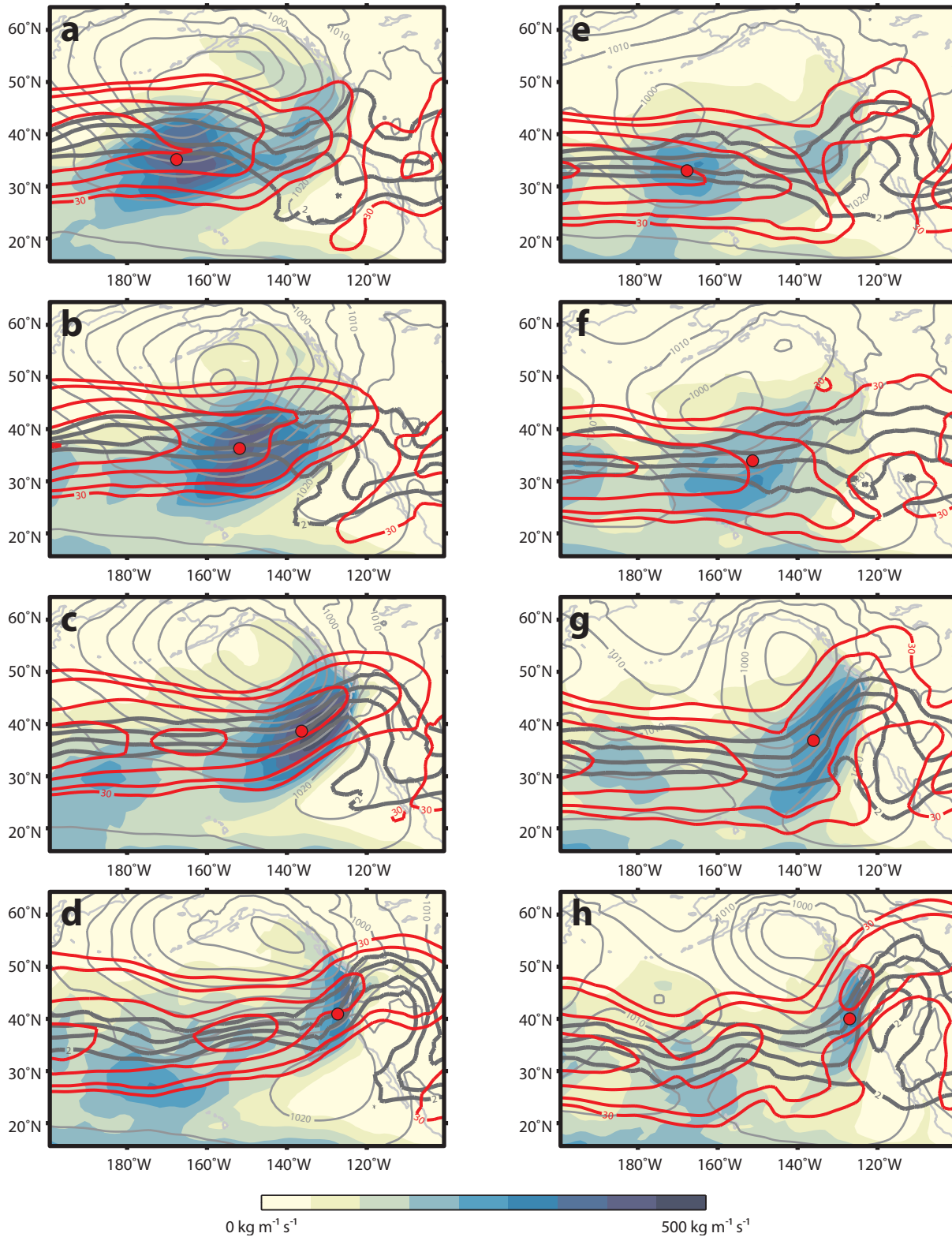


FIG. 10. Same as Fig. 9, but for the (a-d) 11 strongest ARs and (e-h) 11 weakest ARs in our extreme subset for (a,e) 175°–160°W, (b,f) 160°–145°W, (c,g) 145°–130°W and (d,h) 130°–115°W. The average location of the AR centroid is marked by a filled red dot.

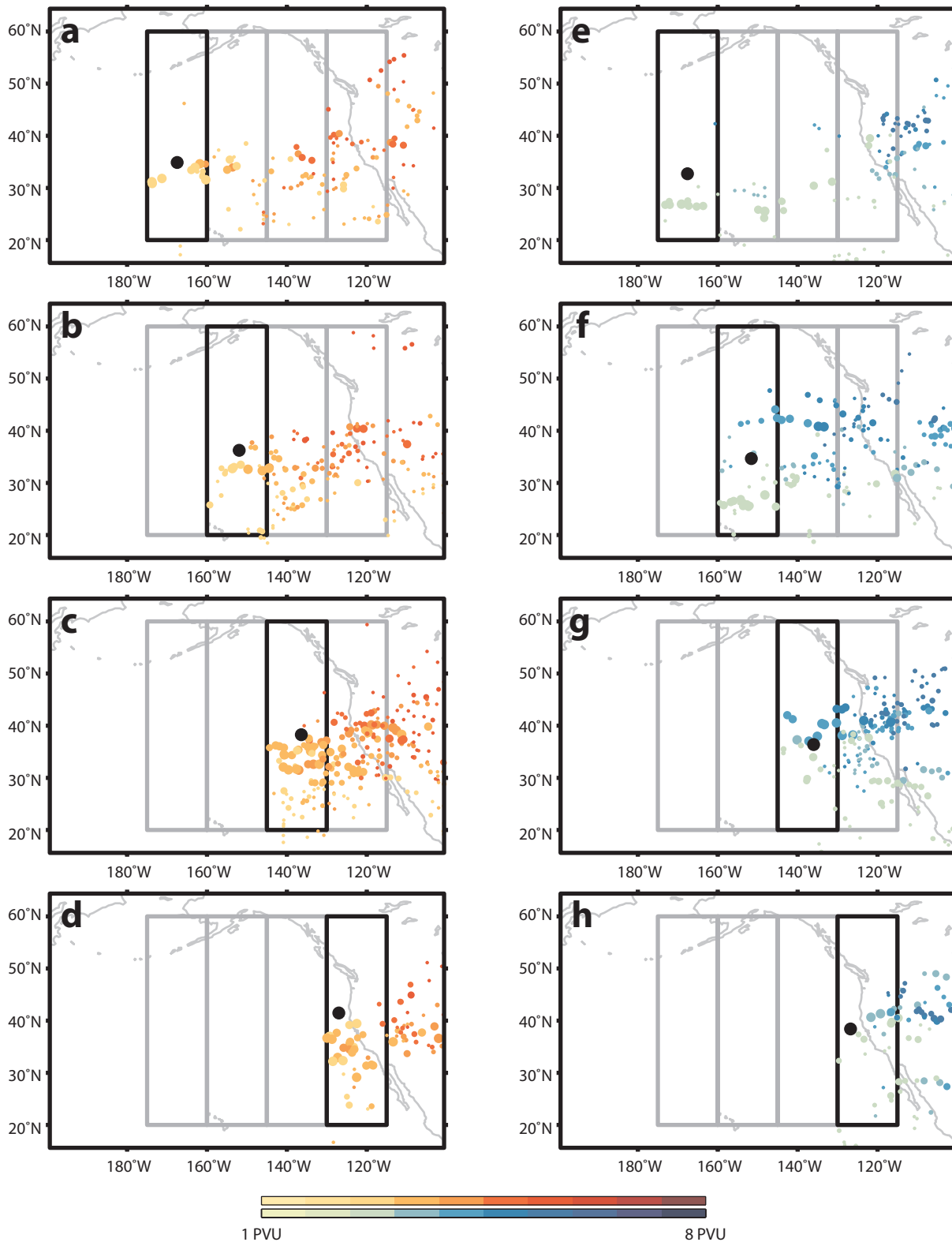


FIG. 11. Relationship between the location of the AR (filled black dot) and anticyclonic RWB for the (a-d) 11 strongest and (e-h) 11 weakest ARs. Using the same regions as in Fig. 9, for each panel, the region the AR is in is outlined in black and all breaking occurring within and leading that region is plotted, where shading indicates the position of breaking (PVU) and size indicates its zonal extent. 45

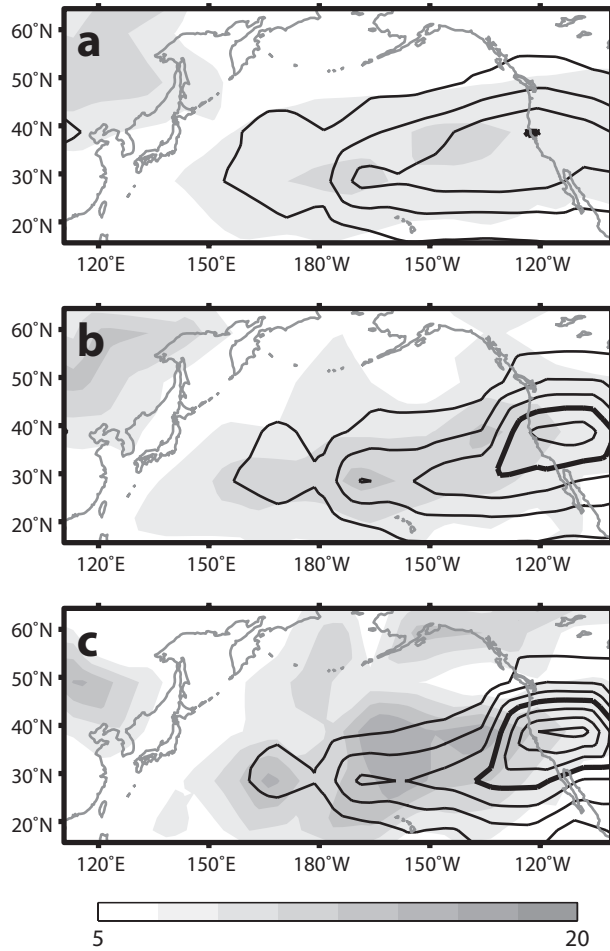


FIG. 12. Anticyclonic RWB relative frequency, γ , (contoured, intervals of 0.05 with the 0.2 contour bolded) and average zonal extent, \bar{L} , (shaded, units of arc length) for (a) the climatological mean of the extended winter over the years 1979 to 2011, (b) all 749 landfalling AR dates over the extended winter over the years 1979 to 2011 and (c) the selected subset of 112 extreme landfalling AR dates.